ISSN 1674-1056
http://cpb.iphy.ac.cn
http://iopscience.iop.org/cpb
中国物理 B
Chinese Physics
中国物理 Chinese Physics B

Investigation and optimization of sampling characteristics of light field camera for flame temperature measurement

Yudong Liu(刘煜东), Md. Moinul Hossain, Jun Sun(孙俊), Biao Zhang(张彪), Chuanlong Xu(许传龙)

Citation: Chin. Phys. B . 2019, 28(3): 034207. **doi:** 10.1088/1674-1056/28/3/034207
Journal homepage: http://cpb.iphy.ac.cn; http://iopscience.iop.org/cpb

What follows is a list of articles you may be interested in

Influence of low-temperature sulfidation on the structure of ZnS thin films

Shuzhen Chen(陈书真), Ligang Song(宋力刚), Peng Zhang(张鹏), Xingzhong Cao(曹兴忠), Runsheng Yu(于润升), Baoyi Wang(王宝义), Long Wei(魏龙), Rengang Zhang(张仁刚)

Chin. Phys. B . 2019, 28(2): 024214. **doi:** 10.1088/1674-1056/28/2/024214

High performance GaSb based digital-grown InGaSb/AlGaAsSb mid-infrared lasers and bars

Sheng-Wen Xie(谢圣文), Yu Zhang(张宇), Cheng-Ao Yang(杨成奥), Shu-Shan Huang(黄书山), Ye Yuan(袁野), Yi Zhang(张一), Jin-Ming Shang(尚金铭), Fu-Hui Shao(邵福会), Ying-Qiang Xu(徐应强), Hai-Qiao Ni(倪海桥), Zhi-Chuan Niu(牛智川)

Chin. Phys. B . 2019, 28(1): 014208. **doi:** 10.1088/1674-1056/28/1/014208

Thermal analysis of GaN-based laser diode mini-array

Jun-Jie Hu(胡俊杰), Shu-Ming Zhang(张书明), De-Yao Li(李德尧), Feng Zhang(张峰), Mei-Xin Feng(冯美鑫), Peng-Yan Wen(温鹏雁), Jian-Pin Liu(刘建平), Li-Qun Zhang(张立群), Hui Yang(杨辉)

Chin. Phys. B . 2018, 27(9): 094208. **doi:** 10.1088/1674-1056/27/9/094208

High-power and high optical conversion efficiency diode-end-pumped laser with multi-segmented Nd: YAG/Nd: YVO_4

Meng-Yao Wu(吴梦瑶), Peng-Fei Qu(屈鹏飞), Shi-Yu Wang(王石语), Zhen Guo(过振), De-Fang Cai(蔡德芳), Bing-Bin Li(李兵斌)

Chin. Phys. B . 2018, 27(9): 094207. **doi:** 10.1088/1674-1056/27/9/094207

Theoretical simulation and analysis of large size BMP-LSC by 3D Monte Carlo ray tracing model

Feng Zhang(张峰), Ning-Ning Zhang(张宁宁), Yi Zhang(张义), Sen Yan(闫森), Song Sun(孙松), Jun Bao(鲍骏), Chen Gao(高琛)

Chin. Phys. B . 2017, 26(5): 054201. **doi:** 10.1088/1674-1056/26/5/054201

Investigation and optimization of sampling characteristics of light field camera for flame temperature measurement*

Yudong Liu(刘煜东)[1], Md. Moinul Hossain[2], Jun Sun(孙俊)[3], Biao Zhang(张彪)[1], and Chuanlong Xu(许传龙)[1,†]

[1] *Key Laboratory of Energy Thermal Conversion and Control of Ministry of Education, School of Energy and Environment, Southeast University, Nanjing* 210096, *China*

[2] *School of Engineering and Digital Arts, University of Kent, Canterbury, Kent, CT2 7NT, UK*

[3] *Sunny Central Research Institute, Hangzhou* 310052, *China*

(Received 16 September 2018; revised manuscript received 31 December 2018; published online 26 February 2019)

It is essential to investigate the light field camera parameters for the accurate flame temperature measurement because the sampling characteristics of the flame radiation can be varied with them. In this study, novel indices of the light field camera were proposed to investigate the directional and spatial sampling characteristics of the flame radiation. Effects of light field camera parameters such as focal length and magnification of the main lens, focal length and magnification of the microlens were investigated. It was observed that the sampling characteristics of the flame are varied with the different parameters of the light field camera. The optimized parameters of the light field camera were then proposed for the flame radiation sampling. The larger sampling angle (23 times larger) is achieved by the optimized parameters compared to the commercial light field camera parameters. A non-negative least square (NNLS) algorithm was used to reconstruct the flame temperature. The reconstruction accuracy was also evaluated by the optimized parameters. The results suggested that the optimized parameters can provide higher reconstruction accuracy for axisymmetric and non-symmetric flame conditions in comparison to the commercial light field camera.

Keywords: light field camera flame radiation sampling, parameter optimization, temperature reconstruction

PACS: 42.15.–i, 44.40.+a, 42.30.Wb, 07.60.Dq **DOI:** 10.1088/1674-1056/28/3/034207

1. Introduction

In the combustion process, the flame temperature is one of the crucial parameters.[1] Because it directly characterizes the combustion burning state, which governs the combustion efficiency and pollutant generation.[2] A precise measurement of the flame temperature is not only crucial to understand the chemical and transport process of combustion but also guides the design of combustion devices such as power plant boilers and industrial furnaces. Therefore, it is desirable to develop an advanced and accurate measurement technique for an in-depth understanding of combustion mechanism and its industrial applications.

To date, various techniques have been proposed and developed for the flame temperature measurement. As an example of the traditional intrusive method, the thermocouple can measure temperature directly from a single point of a flame. However, the temperature distribution of a flame area and the overall burning condition cannot be obtained. Compared to the intrusive technique, the non-intrusive techniques have the advantage of non-interfering with the combustion process, and multi-point measurement can be achieved simultaneously. In principle, the non-intrusive techniques can be classified into active and passive measurement techniques. The active measurement techniques use the laser or ultrasonic signal to measure the flame temperature. With the benefits of high-precision, these methods have been used in many combustion studies.[3,4] However, the spatial resolution of these methods is weak due to a limited number of signal paths. For the three-dimensional (3-D) flame measurement, the active measurement techniques require a large number of signal projections of the flame. As a result, the active measurement techniques suffer complexity setup and higher cost of the system. The passive measurement techniques such as imaging-based methods (known as single-camera/multi-camera systems) utilize flame radiation to reconstruct the temperature distribution through emission tomography and digital image processing techniques. The single-camera system is simple in structure, low cost, and easy to install in large-scale industrial sectors. However, the single-camera system is only suitable for axisymmetric flames and unable to reconstruct unsteady or turbulent combustion conditions.[5,6] The concept of the multi-camera system is based on the optical emission tomography techniques such as filtered back projection (FBP), algebraic reconstruction technique (ART), etc.[7,8] The multi-camera system captures the flame radiative information from different directions around the flame with the aid of multiple cameras/sensors.[8] The radiative information captured from

*Project supported by the National Natural Science Foundation of China (Grant Nos. 51676044 and 51327803), the Social Development Project of Jiangsu Province, China (Grant No. BE20187053), the Postgraduate Research and Practice Innovation Program of Jiangsu Province, China (Grant No. KYCX170081), and China Scholarship Council.

†Corresponding author. E-mail: chuanlongxu@seu.edu.cn

© 2019 Chinese Physical Society and IOP Publishing Ltd

the different directions is then used to reconstruct the 3-D temperature through the emission tomography techniques. However, the complexity and cost of the system are higher due to multiple cameras/sensors compared to the single camera system. Also, due to the complicated calibration, alignment, and synchronization of the multiple cameras/sensors, the multi-camera system is unable to install in large-scale industrial sectors.

As a novel sampling device, the light field camera originated from the light slab parameterization[9] can capture the direction, position, and intensity of each ray of the flame through a single exposure.[10–12] In recent years, the light field camera is applied in combustion to investigate the flame radiation information and reconstruct the 3-D temperature distribution.[13–21] For example, Sun *et al.*[13] proposed a novel algorithm to reconstruct the 3-D temperature distribution of ethylene–air diffusion flames based on the radiative transfer equation and Planck's radiation law, where a commercial focused light field camera (Raytrix R29) was used to sample the flame radiative information. Niu *et al.*[16,17] developed an algorithm to reconstruct the temperature and the radiative properties of a rotationally symmetrical flame using the light field camera. Jeffrey *et al.*[18] also proposed a light field camera system to measure the flame cross-sectional radiative intensity based on a vertical view of the camera and a deconvolution method. Above studies illustrates the practicality of the light field camera for the flame temperature measurement. However, in above studies, the effects of the light field camera parameters on the light field sampling characteristics and the flame temperature measurement were not investigated, though they are crucial to investigate for the accurate and reliable flame temperature measurement.

Various studies were reported to investigate the light field sampling characteristics, but they are mainly focused on the opaque objects such as wood, rock, etc.[22–24] Different parameters of the light field camera and the camera array have also been studied to improve the quality of light field sampling of the opaque object.[11,25] However, the light field flame radiation sampling is fundamentally different from the opaque object. Because the flame is mostly transparent or translucent, so the light emitted from an internal point can penetrate the boundary of the flame.[2] During the light-transmitting process, the flame radiative information would interact with emission, absorption, and scattering effects through its transmitting path and finally reaches a charge-coupled device (CCD) sensor.[26,27] Therefore, each value of the CCD sensor presents an integrated radiation intensity along the transmitting direction of the flame. By using the light field camera, the flame radiation can be sampled from different directions. However, unlike the multi-camera system,[8] the directions sampled by a light field camera can be dense and limited within a small angle. It is challenging to obtain adequate flame radiative information with the smaller sampling angle for the flame measurement.[13,15,17] Because the light field sampling of the flame radiation immensely depends on the parameters of the light field camera.[11,25] Hence, it is essential to investigate the light field camera parameters and sampling characteristics of the light field for the flame measurement.

The main aims of this study are to investigate the sampling characteristics of the light field camera and to optimize the light field camera parameters for the flame temperature measurement. Novel indices of the light field camera such as the cone angle of a single pixel (*CA*), sampling angle (*SA*), spatial resolution (*SR*), and the angle of view (*AOV*) are proposed to characterize the directional and spatial characteristics of the light field sampling. These indices are employed to evaluate the effects of the parameters including the position of the image sensor, the position of the object point, the focal length of the main lens, the magnification of the main lens, the focal length of each microlens, and the magnification of the microlens. The optimized parameters of the light field camera are then proposed for the flame radiation sampling. The backward ray tracing model is used to trace the individual ray sampled by the light field camera and to acquire the light field image. A non-negative least square (NNLS) algorithm is used to reconstruct the axisymmetric and non-symmetric flames temperature distribution. The light field sampling characteristics and the reconstruction accuracy obtained by the optimized parameters are compared with the commercial light field camera parameters. Results obtained from the numerical simulations are presented and discussed in details.

2. Light field sampling of flame radiation

2.1. Principle of the light field imaging

The light field (LF) describes the direction, position, and intensity of the incident light.[9] The position and angle of the incident light can be characterized by two parallel planes using a light field camera (LFC). In the LFC, the two parallel planes are the microlens array (MLA) and the CCD sensor, as shown in Fig. 1. The LFC separates the incident light based on the direction and position of the ray, and thus the incident ray can be captured in a single exposure by the LFC. Based on the locations of the MLA and CCD, the LFC can be categorized into two types, which are the standard LFC and the focused LFC. For the standard LFC, the CCD is located at the focal plane of the MLA (i.e., $f_{\mathrm{m}} = L_{\mathrm{pm}}$), and the MLA is conjugate with the object plane of the main lens. The incident rays coming from an object are converged on the MLA. The incident rays are then separated by the MLA and recorded by the CCD. For the focused LFC, the distance from the MLA to CCD is not equal to the focal length of the microlens (i.e., $f_{\mathrm{m}} \neq L_{\mathrm{pm}}$).[12]

The main lens creates an image of the scene on a virtual image plane. Then the virtual image plane is remapped on the CCD by the MLA, which basically works as a micro camera array. There are two models of the focused LFC such as the Keplerian model and the Galilean model,[28,29] which are categorized based on the position of the virtual image plane. In the Keplerian model, the virtual image plane is in front of the MLA as shown in Fig. 1. In the Galilean model, the virtual image plane is behind the MLA. As a result, the incident rays can reach at the MLA before forming an image on the virtual image plane. It is worth mentioning that all kinds of LFC can be used to record the light field of the flame. However, their sampling characteristics would be different due to the different distances from the MLA to CCD.[12]

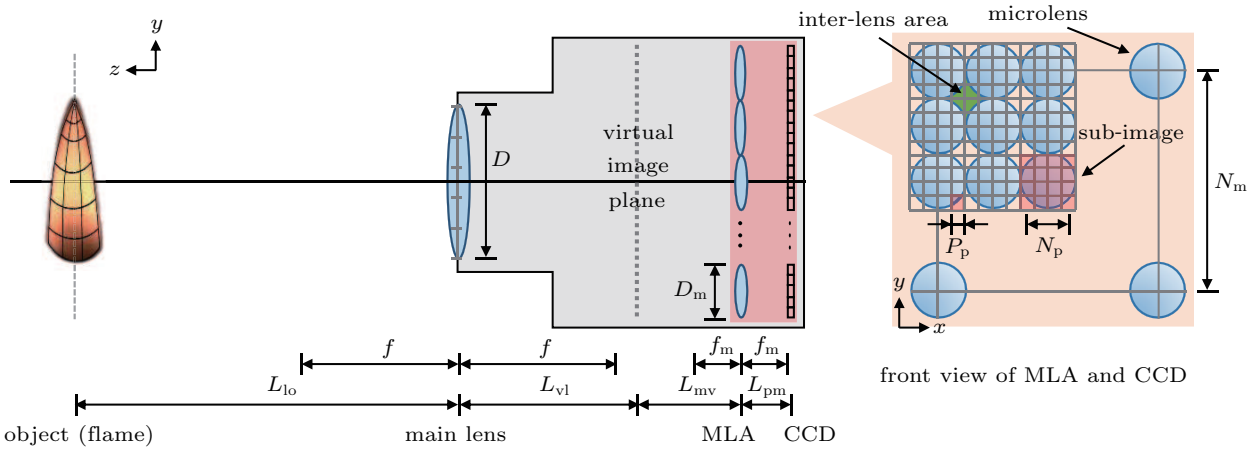


Fig. 1. Schematic of the focused light field camera (Keplerian model).

2.2. Parameters of the light field camera and ray tracing model

The flame radiation captured by the LFC is not only from the flame boundary but also from inside the flame. To investigate the light field sampling characteristics of the flame radiation, numerical simulations were carried out under different parameters of the LFC. The parameters used in the simulations are summarized in Table 1. These parameters are obtained based on the commercial Raytrix's focused LFC (R29). To the best of our knowledge, the Raytrix R29 is the most suitable LFC model for flame measurement in the existing commercial LFCs.[13,14,17,20] The MLA consists of $N_m \times N_m$ microlenses, where each microlens covers by $N_p \times N_p$ pixels. So the diameter of the microlens (D_m) is equal to $N_p \times P_p$ (size of a pixel). It is worth noting that the microlens structure of Raytrix's LFC is hexagonal, while the structure of the study is orthogonal for the purpose of simplifying the analysis. As described in the result section, this simplification does not affect the analysis of the sampling performance. The MLA is mounted in front of the CCD. In the CCD, a sub-division corresponding to a microlens is defined as a sub-image (refer to Fig. 1). The M and M_m are the magnifications of the main lens and the microlens, respectively. The magnification is the ratio of the image size to the object size relate to a lens. For example, in Fig. 1, the magnification of the main lens, M, can be determined by the ratio of the length of the flame image on the virtual image plane to the length of the actual flame. Specifically, the magnification is negative if the object and image planes are on the same side of the lens. The f and f_m are the focal lengths of the main lens and the microlens, respectively. The f_m and M_m are determined by the calibrations and described elsewhere.[15] To investigate the effects of the parameters on the light field sampling, only one parameter is varied during the simulation. The parameters f_m, M_m, f, and M are independent, and their range and interval are determined based on Ref. [30] and summarized in Table 2.

Table 1. Parameters of the commercial light field camera.

Parameter	Value
f_m/μm	769
f/mm	50.0
M_m	−0.2
M	0.11
P_p/μm	15.0
D_m/mm	165
N_m	141

Table 2. Variation ranges of the optical parameters.

Parameter	Range	Interval
f_m/μm	200 –1000	100
M_m	−0.5–+0.5	0.1
f/mm	20–200	20
M	0.1–1.0	0.1

The distance between the CCD and the MLA (L_{pm}) is calculated by

$$L_{pm} = (M_m + 1) \times f_m. \quad (1)$$

The distance between the MLA and the virtual image plane ($L_{\rm mv}$) is determined by

$$L_{\rm mv} = \begin{cases} \dfrac{1}{1/f_{\rm m} - 1/L_{\rm pm}}, & M_{\rm m} \neq 0, \\ 0, & M_{\rm m} = 0, \end{cases} \tag{2}$$

where $M_{\rm m} = 0$ denotes the standard LFC. The distance between the virtual image plane and the main lens ($L_{\rm vl}$) is calculated by

$$L_{\rm vl} = (M+1) \times f. \tag{3}$$

The distance between the main lens and the object plane ($L_{\rm lo}$) is obtained by Gaussian lens formula[28]

$$L_{\rm lo} = \frac{1}{1/f - 1/L_{\rm vl}}. \tag{4}$$

The exit pupil diameter of the main lens (D) is calculated based on the F-number matching equation[11]

$$D = k \times D_{\rm m} \times \frac{L_{\rm mv} + L_{\rm vl}}{L_{\rm pm}}, \tag{5}$$

where the factor k is introduced into the F-number matching equation to ensure that the edge between two adjacent sub-images is larger than an individual pixel. The k is determined by

$$k = \begin{cases} 1 - \dfrac{L_{\rm vl}}{M_{\rm m} \times (L_{\rm mv} + L_{\rm vl})}, & M_{\rm m} \neq 0, \\ 1, & M_{\rm m} = 0. \end{cases} \tag{6}$$

The parameters $L_{\rm pm}$, $L_{\rm mv}$, $L_{\rm vl}$, $L_{\rm lo}$, and D can be determined by Eqs. (1)–(5) based on the parameters illustrated in Tables 1 and 2.

The coordinate system utilized in this study is illustrated in Fig. 4, and the center of the CCD plane is considered as the origin point (0, 0, 0). The backward ray tracing model is used to trace the incident ray corresponding to an individual pixel based on the principle of geometric optics.[28] In the ray tracing process, the ray originating from an individual pixel passes through a specific point of the microlens, the main lens, and finally be cast on the object space.

2.3. Light field sampling of flame radiation and representative ray

In the ray tracing process, a large number of rays can be traced from an individual pixel and then be directed to the object space in different directions. In Subsection 2.2, it has been illustrated that all rays from an individual pixel pass through the same area of the object plane and they are conjugated to the pixel. Thus the rays corresponding to an individual pixel are regarded as an inseparable set of rays and can be defined as an individual light field sampling (i.e., LF sampling) as shown in Fig. 2. In the object space, the volume of ray transmitting path corresponding to an individual LF sampling is basically a cone, and the cone is located on the main lens plane. For the flame radiation sampling, the radiative intensity within the cone can be recorded by the corresponding pixel. In this study, the concept of the representative ray is defined and utilized to characterize the LF sampling (red line in Fig. 2). The position and direction of the representative ray are the mean values of all rays corresponding to the individual LF sampling. So the representative ray can present the direction and position of the corresponding LF sampling.

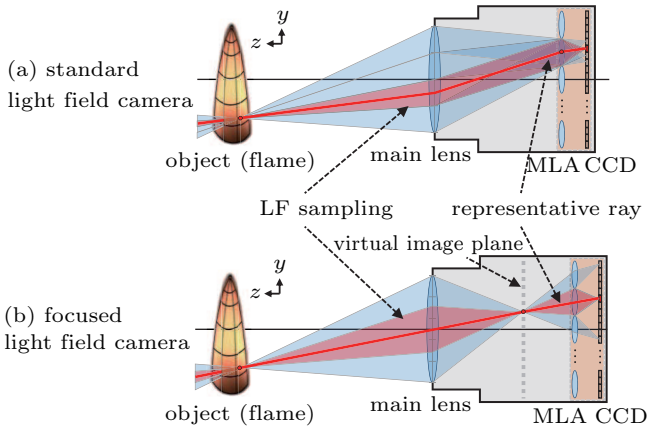


Fig. 2. Schematic of flame radiation sampling of the light field camera.

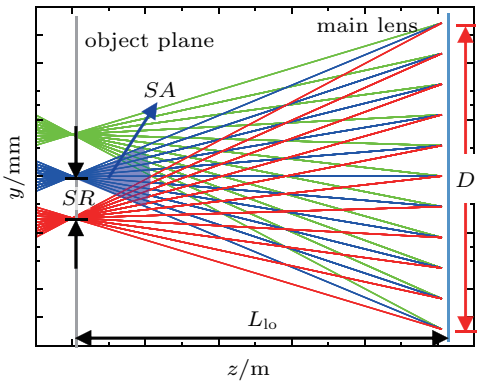


Fig. 3. Example of the distribution of representative rays for three adjacent object points.

Figure 3 illustrates the example of the distribution of the representative rays. In this figure, the representative rays obtained from three adjacent points are drawn in red, green, and blue on the y–z plane. Also, the gray and blue dash lines denote the object and main lens planes, respectively. The height covered by all rays is equal to the diameter of the main lens D. It can be seen that the distribution of the representative rays illustrates the number, position, and direction of LF samplings from an individual point. It is worth noting that the distribution of the representative rays depends on the parameters of LFC such as the focal length and magnification of the main lens, and the focal length and magnification of the microlens.

To characterize the light field sampling quantitatively, a series of sampling indices have been proposed and calculated in this study.

2.4. Directional sampling indices

To characterize the directional sampling characteristics of the flame, the directional sampling indices including the cone angle of a single pixel (*CA*) and the sampling angle (*SA*) of the object side have been proposed and defined in this study. In Fig. 4, *CA* and *SA* are defined as the red cone and the blue cone, respectively.

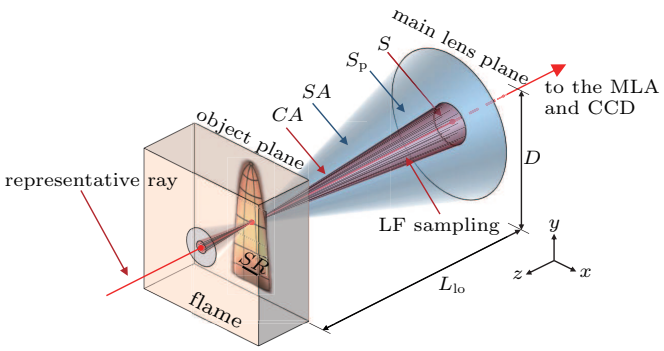


Fig. 4. Directional sampling indices of light field camera for the flame.

The cone angle of a single pixel (*CA*) is the solid angle corresponding to the rays collected by an individual LF sampling. Based on geometric optics, *CA* can be calculated by

$$CA = \frac{S \times \sin(\theta) \times \cos(\varphi)}{r^2}, \tag{7}$$

where S is the intersection of the cone with the main lens plane, r is the radial distance from the main lens plane to the object plane, θ is the polar angle, and φ is the azimuth angle of a representative ray of the red cone in the spherical coordinate system. The directional sampling accuracy of the representative ray corresponding to an individual LF sampling can be characterized by the *CA*. Note that the smaller *CA* indicates that the direction of all rays in the cone is closer to the representative ray. Thus, the flame intensity corresponding to a pixel can represent the LF sampling more accurately.

The sampling angle (*SA*) is the solid angle of the cone corresponding to all rays collected from an individual point. The *SA* can be calculated by

$$SA = \frac{S_p \times \sin(\theta_p) \times \cos(\varphi_p)}{r_p^2}, \tag{8}$$

where S_p denotes the area covered by all the rays on the pupil plane of the main lens, r_p is the radial distance, θ_p is the polar angle, and φ_p is the azimuth angle of the representative ray of the blue cone in the spherical coordinate system. The *SA* characterizes the adequacy of the directional sampling. The larger *SA* means that the more LF samplings can be obtained from the individual point of the flame, and thus the flame temperature can be reconstructed more accurately.

2.5. Spatial sampling indices

The spatial resolution (*SR*) and the angle of view (*AOV*) have been defined and illustrated in this study to characterize the LF spatial sampling. In the CCD sensor, a square pixel is conjugate to a square area on the object plane (in Fig. 4). The distance between two adjacent square areas is defined as the spatial resolution (*SR*). Based on the thin lens theory,[28] *SR* is calculated by

$$SR = \begin{cases} \dfrac{P_p \times L_{pm} \times L_{vl}}{L_{mv} \times L_{lo}}, & M_m \neq 0, \\ L_{lo} \times \dfrac{D_m}{L_{mv} + L_{vl}}, & M_m = 0, \end{cases} \tag{9}$$

where L_{pm}, L_{mv}, L_{vl}, L_{lo}, and D_m are calculated using Eqs. (2)–(5), and P_p is the size of a pixel. The *SR* characterizes the LFC spatial resolution of the object points. The smaller *SR* means that the spatial sampling will be dense and the more detailed spatial information can be obtained. The angle of view (*AOV*) characterizes the field of view of the LFC. Based on the intercept theorem,[28] *AOV* can be calculated by

$$AOV = 2 \times \arctan\left(\frac{P_p \times N_m \times N_p}{2 \times (l_{mv} + l_{vl})}\right). \tag{10}$$

The greater *AOV* means that the wider view of the object can be captured.

Based on the aforementioned definition of the directional and spatial sampling indices, the effects of the LFC parameters on sampling characteristics of the flame are investigated and discussed in next section.

3. Results and discussion

3.1. Effects of pixel position on the CCD

Figure 5 shows the variation of *CA* with the pixel position on the CCD sensor. The variation is obtained based on the LFC parameters listed in Table 1. It can be seen that the *CA* corresponding to all pixels is rotationally symmetric as shown in Fig. 5(a). Also, the *CA* decreases from the central pixel (maximum) to boundary pixel but, microscopically, the *CA* is not continuous with the pixel because some pixels are located in the inter-lens area (refer to Fig. 1), and they are not covered by sub-images. Thus no radiative information can be received by these pixels. It has been observed that the *CA* is varied with different sub-images. The central sub-image is rotationally symmetric, whose central point is on the optical axis of the main lens (z-axis). For the off-z-axis sub-images, the *CA* increases with the increasing distance between the pixel and the optical axis of the main lens, as shown in Fig. 5(b). This is due to the inconsistency of the relative position of the pixel, microlens, and the optical axis of the main lens. When the

microlens is away from the optical axis of the main lens, the visible area of the main lens pupil is decreased due to the cosine effect.[28] As a result, the vertical sectional area of the incident rays within the LF sampling is decreased, and hence the *CA* is decreased from the central pixel to boundary pixel. It can be seen that the *CA* decreases from 3.58×10^{-5} sr (maximum at center) to 3.33×10^{-5} sr (minimum at the edge) as shown in Fig. 5(b). The mean value of all *CA*s is found $CA_{\mathrm{m}} = 3.49 \times 10^{-5}$ sr. The normalized differences (Δ) of *CA* corresponding to the single pixel is calculated by

$$\Delta = \frac{|CA - CA_{\mathrm{m}}|}{CA_{\mathrm{m}}} \times 100\%. \tag{11}$$

It has been found that the normalized differences of *CA* corresponding to the center and edge pixels are 2.3% and 4.6%, respectively. This is suggested that the LFC provides uniform directional sampling for all pixels, and the representative ray is capable of representing the directional sampling accurately for the flame.

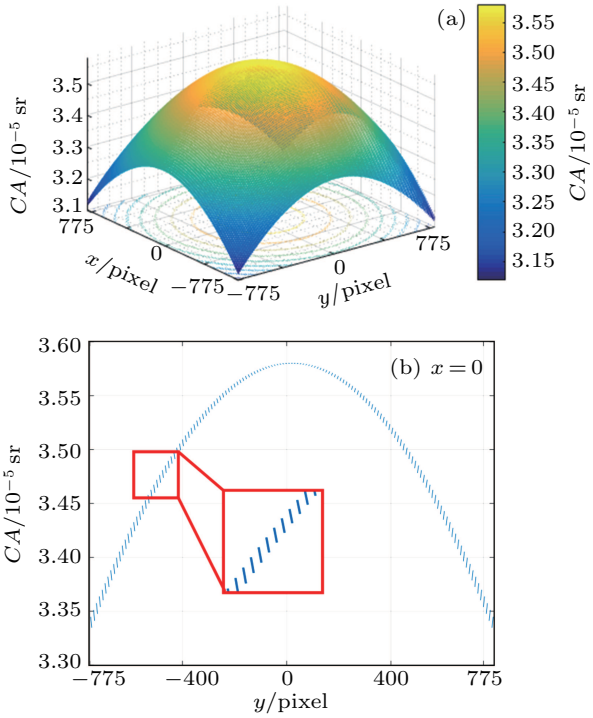


Fig. 5. (a) Distribution of *CA* with the positions of the pixels. (b) The distribution of *CA* corresponding to a column of pixels (i.e., $x = 0$).

Figure 6 shows the variation of *SA* with the position of the object point. The *SA* variation is obtained based on the parameters illustrated in Table 1. It has been observed that the *SA* has the rotational symmetry where the maximum is in the central object point, and the minimum is in the corner object point as shown in Fig. 6(a). It can be seen that the distribution of *SA* is continuous because the sampling of object points is continuous, which is different from the discrete distribution of *CA*. Due to vignetting effects, the distribution of *SA* fluctuates periodically. The normalized difference (δ) of *SA* corresponding to each object point is calculated by

$$\delta = \frac{|SA - SA_{\mathrm{m}}|}{SA_{\mathrm{m}}} \times 100\%. \tag{12}$$

The normalized differences of *SA* corresponding to the center and the edge point are observed 2.5% and 4.5%, respectively. Thus it demonstrates that the sampling angle of each object point is almost uniform within the field of view. However, the angle of rays that an LFC can collect is smaller if the *SA* is smaller. It means that the directional sampling can be lower and inadequate for the flame temperature reconstruction. Hence, it is crucial to get larger *SA* for adequate directional sampling. The larger *SA* can only be achieved by optimizing the LFC parameters.

The *SR* and *AOV* are calculated by using the parameters D_{m}, L_{mv}, L_{vl}, L_{lo}, p_{p}, N_{m}, and N_{p} as discussed in Subsection 2.5, which means they are not related to the position of each pixel or the object point. For the commercial LFC parameters (Table 1), the *SR* and *AOV* are found 681.8 μm and 24.3°, respectively.

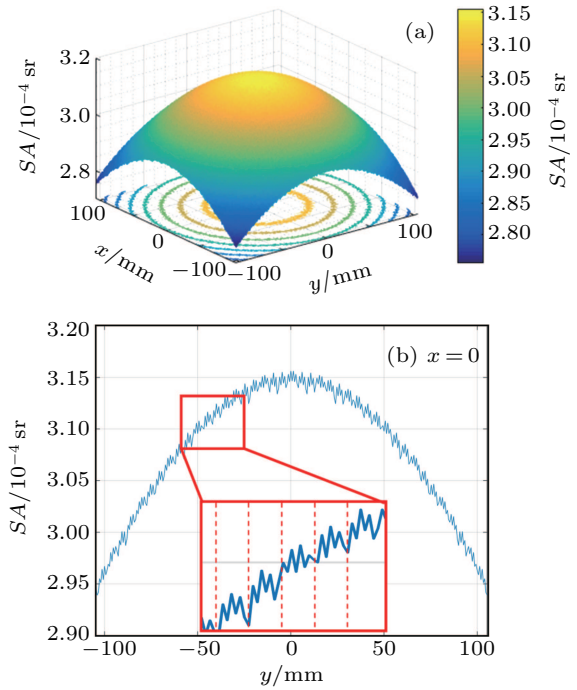


Fig. 6. (a) Distribution of *SA* with the positions of object points. (b) The distribution of *SA* corresponding to a column of object points (i.e., $x = 0$).

3.2. Effects of the magnification of the microlens

Figure 7 shows the variation of the sampling indices (*CA*, *SA*, *SR*, and *AOV*) with the magnifications of the microlens (M_{m}). It is found that the distributions of *CA* and *SA* are rotationally symmetric, so only the distributions of the center and edge pixels of *CA* and *SA* are calculated and illustrated. From Fig. 7(a), it can be seen that the *CA* decreases and then increases significantly with the increasing M_{m}. The lowest $CA = 1.83 \times 10^{-6}$ sr is observed at $M_{\mathrm{m}} = 0$ (standard

LFC). It can also be seen that the *SA* decreases with increasing M_m except $M_m = 0$, as shown in Fig. 7(b). The higher *SA* (3.84×10^{-4} sr) is found at $M_m = 0$. Both the *CA* and *SA* are lower at the edge pixel compared to the center pixel, which is consistent with the results presented in Figs. 5 and 6. The variations of *SR* and *AOV* with different magnifications of the microlens are shown in Figs. 7(c) and 7(d). The maximum *SR* (i.e., 1.48 mm) and the smallest *AOV* (23.7°) are observed at $M_m = 0$. The maximum *SR* at $M_m = 0$ indicates the lower spatial resolution which can create a significant error in the flame temperature reconstruction.

Therefore, it is evident that different sampling characteristics can be obtained between the standard LFC ($M_m = 0$) and the focused LFC ($M_m \neq 0$). For the focused LFC, the *CA* and *SA* are higher for the negative M_m in comparison to the positive M_m. It indicates that larger sampling angle and lower accuracy of the directional sampling can be obtained with the negative M_m, and the maximum *SA* and *SR*, and the minimum *CA* and *AOV* can be achieved for the standard LFC. Therefore, it is clear that better accuracy of the directional sampling and a larger sampling angle can be obtained by the standard LFC. In contrast, better spatial resolution and greater field of view are achieved by the focused LFC. This can be explained by the trade-off between the directional sampling ability and the spatial sampling ability.[12] Hence, for the reconstruction of axisymmetric flames, the focused LFC would be useful because of the higher spatial resolution[15–17] and because adequate directional sampling is not required. However, for the accurate reconstruction of non-symmetric flames, adequate directional sampling and a larger sampling angle are required due to the complex structure of the non-symmetric flames. Based on the above results, it can be concluded that the standard LFC would be better for the non-symmetric flames.

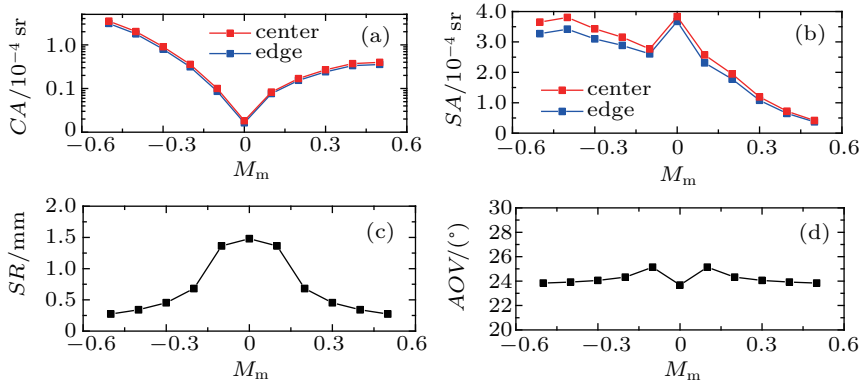


Fig. 7. Variations of the sampling indices with the magnifications of microlens (M_m): (a) *CA*, (b) *SA*, (c) *SR*, (d) *AOV*.

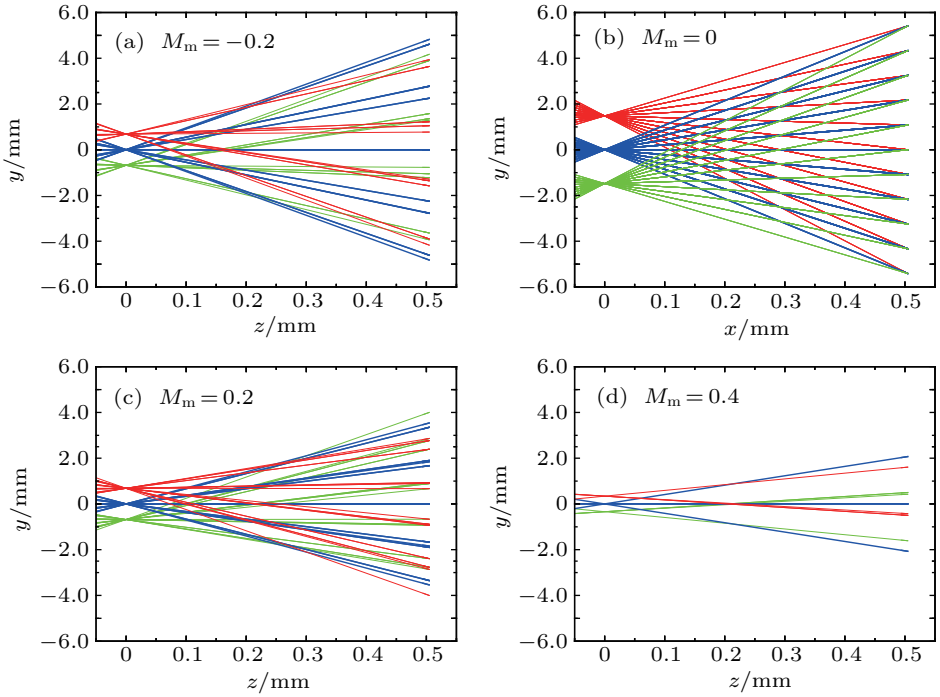


Fig. 8. Distributions of the representative rays with the magnification of microlens: (a) $M_m = -0.2$, (b) $M_m = 0$, (c) $M_m = 0.2$, (d) $M_m = 0.4$.

Further to explain the light field sampling characteristics of the flame, the distributions of representative rays are presented and shown in Fig. 8. It can be seen that more representative rays from the single point are obtained by the standard LFC as shown in Fig. 8(b). Hence, for the standard LFC, more directional sampling can be achieved. Also, the representative rays are uniformly distributed and covered by a larger sampling angle. On the contrary, fewer representative rays are obtained by the focused LFC, and they are not uniformly distributed. Also, the total number of representative rays is decreased significantly with the increasing M_{m}, as shown in Figs. 8(c) and 8(d). Based on the definition of *SR* as shown in Fig. 3, it can be seen that the larger *SR* is at $M_{\mathrm{m}} = 0$ (Fig. 8(b)). The sampling angle covered by the representative rays is also decreased, and the trend is consistent with the result illustrated in Fig. 7(b).

3.3. Effects of the focal length of the microlens

Figure 9 illustrates the variation of sampling indices with the focal length of the microlens (f_{m}). It can be seen that the *CA* and *SA* decrease significantly with increasing f_{m} as shown in Figs. 9(a) and 9(b). As a result, the sampling angle can be increased due to a smaller f_{m}, but the accuracy of directional sampling will be decreased. Besides, constant variation of *SR* and *AOV* is observed as shown in Figs. 9(c) and 9(d). It indicates that no effect can be made on the spatial sampling characteristics (*SR* and *AOV*) due to the change of f_{m}. Hence, for the *SA* and *CA*, it is crucial to select an appropriate focal length of the microlens for the directional sampling of the flame radiation.

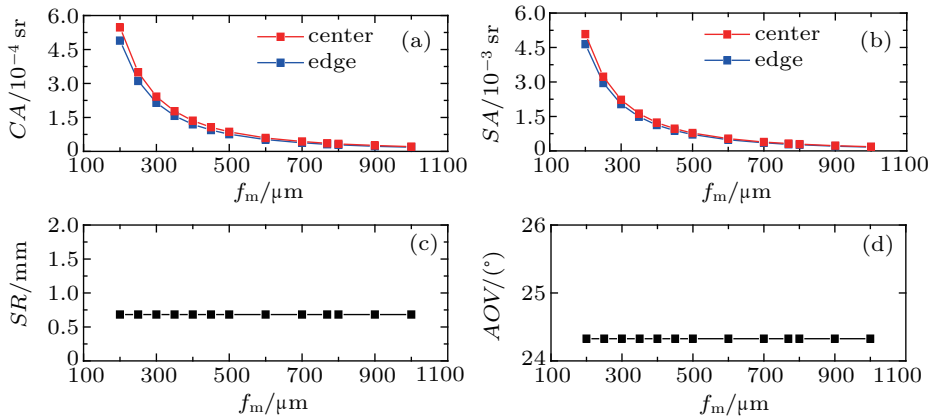


Fig. 9. Variations of the sampling indices with the focal length of the microlens: (a) *CA*, (b) *SA*, (c) *SR*, (d) *AOV*.

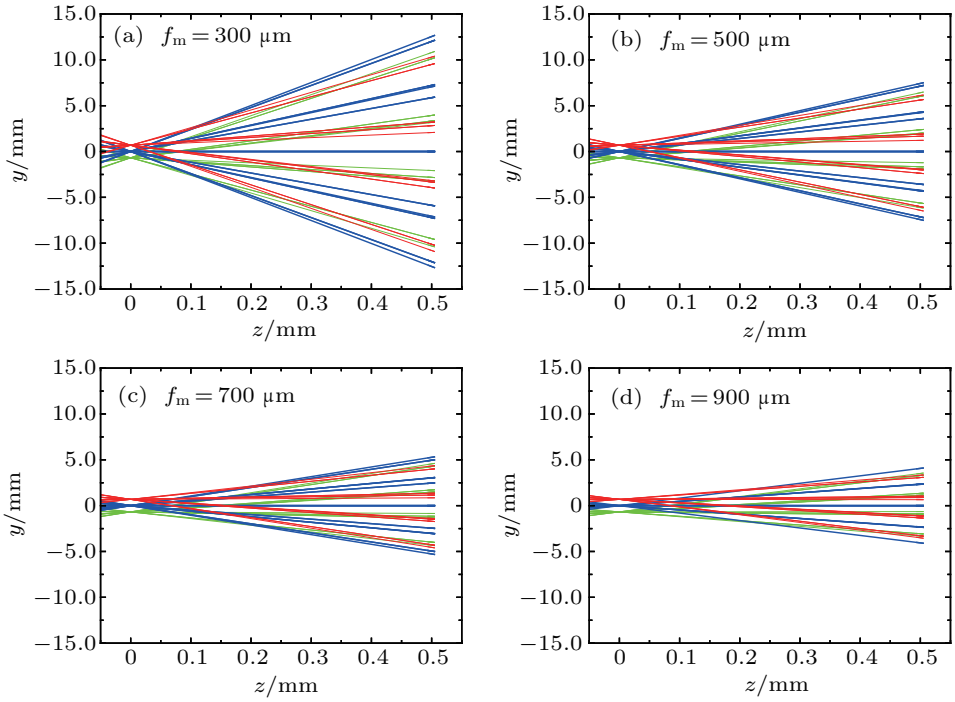


Fig. 10. Distributions of representative rays with the different focal lengths of the microlens: (a) $f_{\mathrm{m}} = 300$ μm, (b) $f_{\mathrm{m}} = 500$ μm, (c) $f_{\mathrm{m}} = 700$ μm, (d) $f_{\mathrm{m}} = 900$ μm.

Figure 10 shows the distribution of representative rays with different focal lengths of the microlens (f_m). It can be seen that the sampling angle (*SA*) covered by the representative rays is decreased with the increasing f_m as shown in Figs. 10(a)–10(d). It is because the *SA* is determined by the base area (S_p) of the cone, which is affected by the pupil diameter of the main lens (D). And D is decreased with the increasing f_m. It can also be seen that the *SR* is not changed with f_m. It indicates that the larger sampling angle can be achieved by a smaller f_m, but the spatial sampling resolution would be the same. Besides, the non-uniform distribution of the representative rays is observed for all the focal lengths. It further proves that the focused LFC provides the non-uniform distribution of the directional sampling.

3.4. Effects of the magnification of the main lens

Figure 11 shows the variation of the sampling indices with the magnification of the main lens (M). It can be seen that the *CA* and *SA* are increased with the increase of M, as shown in Figs. 11(a) and 11(b). Also, the *SR* and *AOV* are decreased significantly with the increase of M as illustrated in Figs. 11(c) and 11(d). So it can be concluded that the magnification of the main lens has a significant impact on the sampling indices, the increase of M leads to a larger sampling angle and better spatial resolution but lower accuracy of directional sampling and smaller field of view. To capture a large-scale furnace flame, a lower M should be selected to increase the *AOV*. However, the problem is that the sampling angle and spatial resolution would be deteriorated, and the directional sampling could be inadequate for the flame reconstruction.

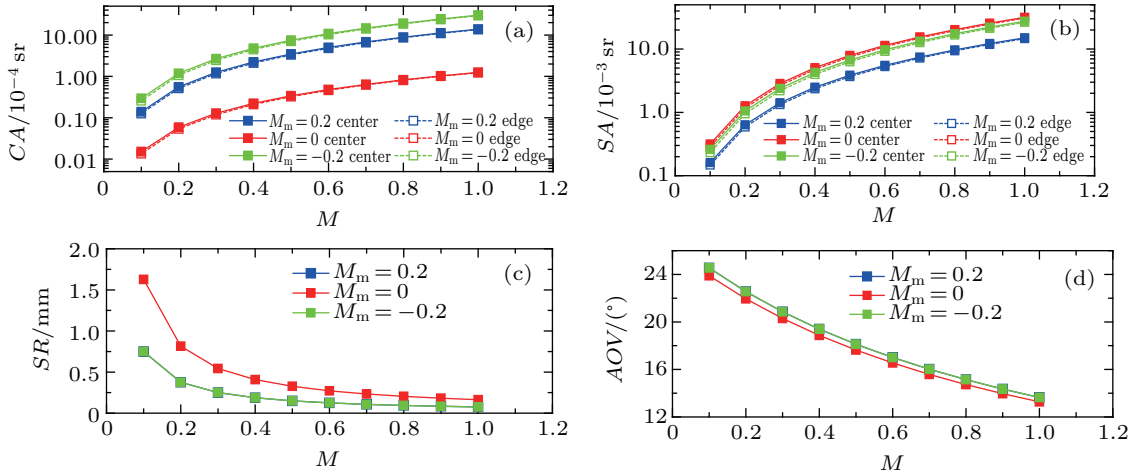


Fig. 11. Variations of the sampling indices with the magnification of the main lens: (a) *CA*, (b) *SA*, (c) *SR*, (d) *AOV*.

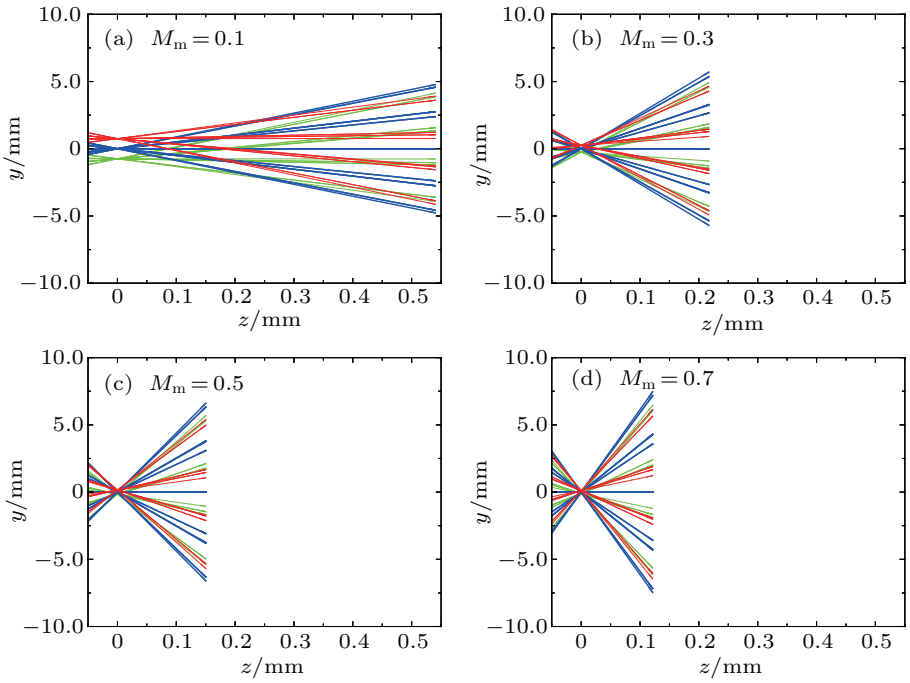


Fig. 12. Distributions of the representative rays with the magnification of the main lens: (a) $M = 0.1$, (b) $M = 0.3$, (c) $M = 0.5$, (d) $M = 0.7$.

Besides, the lowest *CA* and the highest *SA* are found for the standard LFC ($M_m = 0$) compared to the focused LFC particularly at $M_m = 0.2$ and -0.2 (Figs. 11(a) and 11(b)). It indicates that better accuracy of directional sampling and larger sampling angle can be achieved by the standard LFC but the standard LFC provides the lower spatial resolution for each object point. The focused LFC with positive M_m provides lower *CA* and *SA* compared to the negative M_m. Therefore, more accurate directional sampling can be achieved by the focused LFC with positive M_m, but the sampling angle would be smaller. The trend is consistent with the results presented in Fig. 7.

Figure 12 illustrates the distribution of representative rays with the magnification of the main lens (M). It can be seen that the distance between the object plane and the main lens (L_{lo}) is significantly decreased with the increase of M where the diameter of the exit pupil of the main lens (D) is unchanged. Hence, the sampling angle (SA) covered by all representative rays is increased with increasing M. Hence, a larger sampling angle can be achieved by the increasing M, but the distance between the flame and the LFC could be decreased simultaneously. As a result, both the focused LFC and standard LFC are able to record adequate information for the small-scale flame using the larger M and the shorter distance between the flame and the LFC.

3.5. Effects of the focal length of the main lens

The effects of the focal length of the main lens are also investigated. Figure 13 depicts the variations of the sampling indices with the focal length of the main lens (f). No significant variations are observed for the *CA* and *SA*. Also no changes have been seen for the *SR* with the different focal lengths (f). Variations are only found for the *AOV* which is decreased significantly with the increasing f, as shown in Fig. 13(d). It indicates that the larger *AOV* can be achieved by the smaller f such as 24 mm. Hence, a smaller f and larger *AOV* would be suitable to capture a larger area of the flame such as a large-scale industrial flame.

Further to investigate the effects of the focal length of the main lens (f), the distribution of the representative rays is also presented in Fig. 14. It can be seen that the distance between the object plane and the main lens (l_{lo}) is increased with the increasing f and thus the diameter of the exit pupil of the main lens (D) is increased simultaneously. As a result, the sampling angle covered by all the representative rays remains unchanged with the f. Therefore, no significant changes can be seen in the sampling characteristics.

Based on the above results and discussion, the remarkable observations are summarized as follows.

(I) Firstly, significant changes are seen for the *AOV* with the magnification and focal lengths of the main lens. However, the sampling indices of *CA*, *SA*, and *SR* are not affected by the focal length. So the appropriate *AOV* can be achieved by changing the focal length independently.

(II) Secondly, remarkable changes are seen for the *SA* with the focal lengths of the microlens and the magnification of the main lens. Hence, the *SA* can be increased by decreasing the focal length of the microlens and increasing the magnification of the main lens. Although the changing of the focal length of the microlens and the focal length of the main lens can affect the sampling indices of *CA* and *SR*.

(III) Lastly, the *CA* can be minimized and the higher *SR* can be achieved with the magnification of the microlens equaling zero (standard LFC).

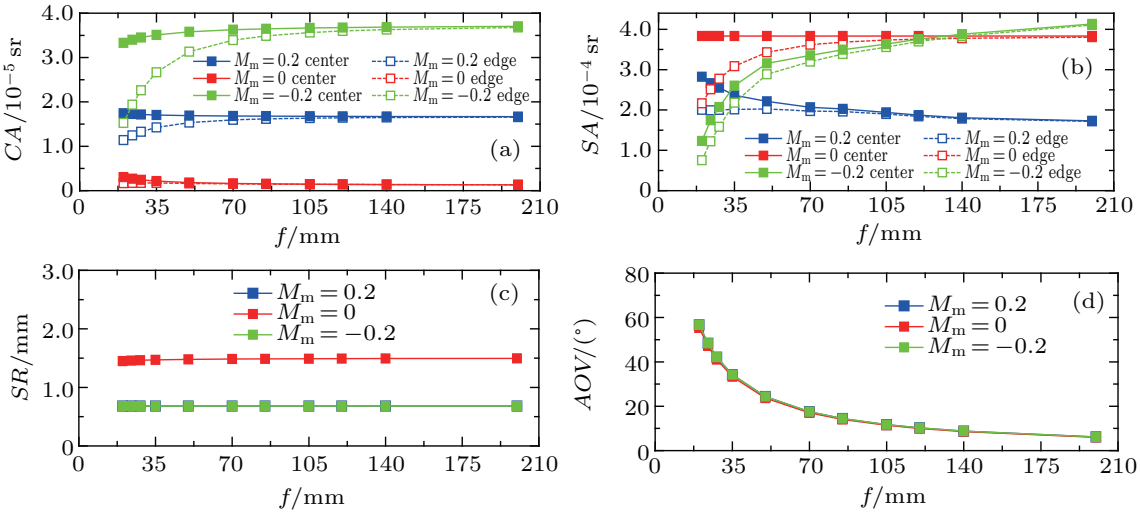


Fig. 13. Variations of the sampling indices with the focal length of the main lens: (a) *CA*, (b) *SA*, (c) *SR*, (d) *AOV*.

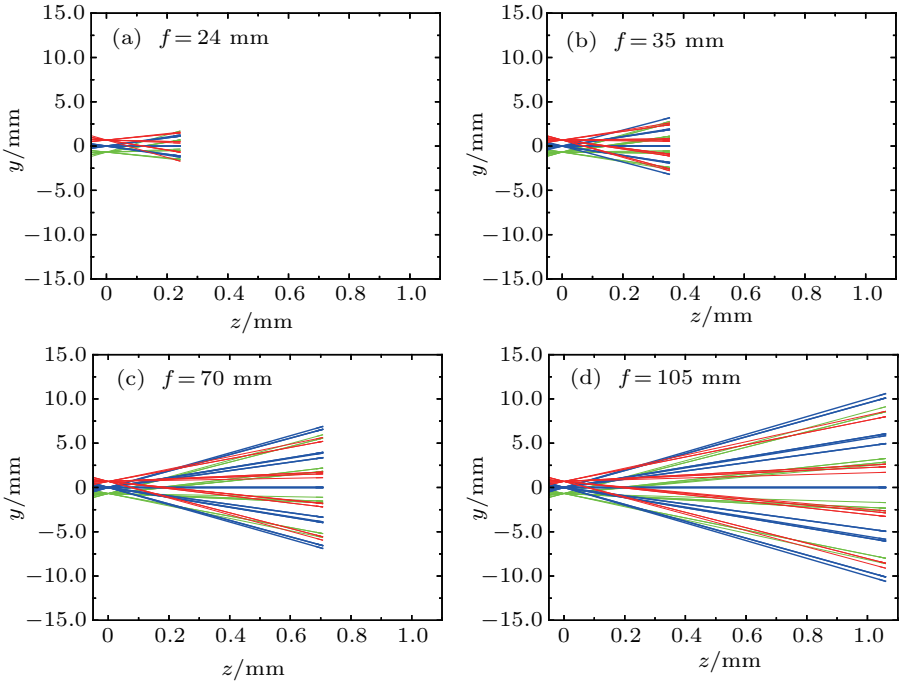


Fig. 14. Distributions of the representative ray with the focal length of the main lens: (a) $f = 24$ mm, (b) $f = 35$ mm, (c) $f = 70$ mm, (d) $f = 105$ mm.

3.6. Proposed parameters of the light field camera

To investigate and optimize the light field sampling for the flame reconstruction, the sampling characteristics of the commercial LFC are investigated based on the parameters illustrated in Table 1. Figure 15(a) illustrates the distribution of the representative rays of the commercial LFC. Relatively lower sampling angle and a lower number of representative rays are observed, which indicates that the lower directional sampling could be inadequate for the flame reconstruction. Besides, the non-uniform distribution of the directional sampling is also found as shown in Fig. 15(a). As a result, the reconstruction accuracy would be lower especially for the non-symmetric flame.[13] Also, a smaller field of view has been seen in Subsection 3.1 for the commercial LFC, which may not be suitable for the large-scale flames.

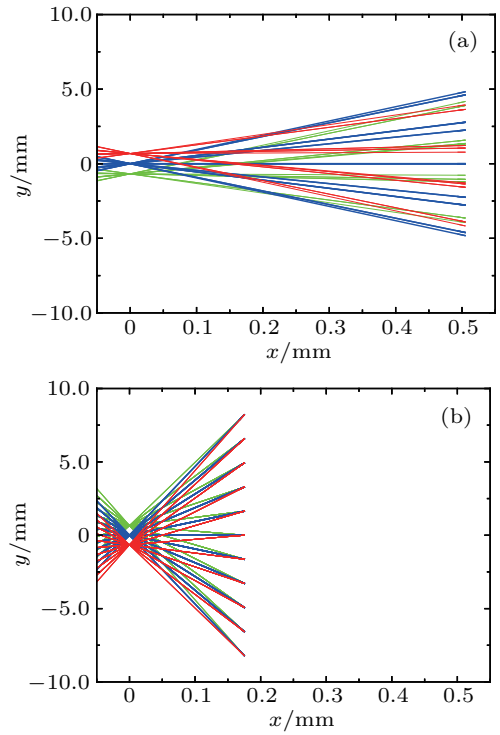


Fig. 15. Distributions of the representative ray of (a) commercial and (b) optimized LFCs.

Therefore, to improve the performance of the light field sampling for the flame reconstruction, firstly, it is crucial to increase the sampling angle to acquire adequate samples of rays. It is because adequate samples can increase the reconstruction accuracy. Secondly, to ensure the applicability of the various sizes of the flame, a wider field of view is needed. Further to improve the reconstruction accuracy of the flame, it is useful to improve the directional sampling accuracy and also to achieve a higher spatial resolution.

Considering the aforementioned results and discussion, the optimized parameters of the LFC are proposed for the flame reconstruction and summarized in Table 3. The sampling characteristics are then investigated based on the optimized parameters. Figure 15(b) shows the distribution of the representative rays for the LFC of the optimized parameter. The larger sampling angle is achieved by the optimized parameters compared to the commercial LFC parameters. The sampling indices of CA, SA, SR, and AOV are calculated using the optimized parameters and then compared with those obtained using the commercial LFC parameters. The ratios of sampling indices between the optimized parameters and the commercial LFC are shown in Fig. 16. In the figure, the blue

dash line is the ratio (= 1) of the indices of the commercial LFC. It can be seen that the optimized parameters of LFC provide improvements in all the four sampling indices, which are the larger *AOV* and *SA*, smaller *CA* and *SR*. Specifically, the *SA* is improved significantly, which is ~23 times higher than that of the commercial LFC. As a result, adequate directional sampling information can be achieved by the optimized parameters. It can be concluded that the reconstruction accuracy can be improved by the optimized parameters of the LFC and thus accurate measurement can be obtained.

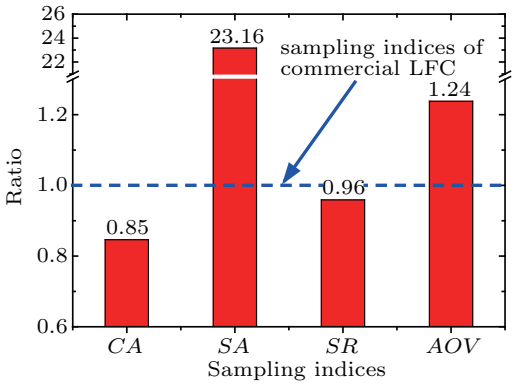


Fig. 16. The ratio of the indices of optimized and commercial LFCs.

Table 3. Commercial and optimized parameters of the light field camera.

Parameter	Commercial LFC	Optimized LFC
f_{m}/μm	769	400
M_{m}	−0.2	0.0
f/mm	50	35
M	0.11	0.25

3.7. Reconstruction of flame temperature

In order to evaluate the optimized parameters of the LFC, numerical simulations are carried out for the flame temperature reconstruction. In this study, a cylindrical flame is considered for the numerical simulation, the radius and height of the cylindrical flame are set to 8 mm and 30 mm, respectively. Two different flame temperature distributions are considered in the simulation to verify the applicability of the proposed parameters. The flame of T_1 is axisymmetric, which is based on the ethylene diffusion flame as[20,31]

$$T_1(x,y,z) = 1200\exp\left\{-\left[3\left(\frac{z^2}{Z^2}+\frac{x^2+y^2}{R^2}\right)-0.9\right]^2\right\} + 900\ (\mathrm{K}). \tag{13}$$

The flame of T_2 is non-symmetric and defined based on Ref. [16] as

$$T_2(x,y,z) = \frac{2200}{3}\exp\left[-40\left(\frac{750x+7.5}{9}-1.1\right)^2 - 25\left(\frac{750y+8.5}{9}-0.8\right)^2\right] + \frac{1760}{3}\exp\left[-25\left(\frac{750x+7.5}{9}-0.8\right)^2 - 35\left(\frac{750y+8.5}{9}-1.2\right)^2\right] + \frac{88000}{3}z+1633\ (\mathrm{K}). \tag{14}$$

Here x, y, and z are the system coordinates. The flame absorption coefficient of 8 m^{-1} is used in this study which is investigated in Refs. [17], [31], and [32]. It should be noted that if the flame is very sooty, the absorption coefficient might be different and not uniform. The scattering effect is neglected because the scattering effect of soot in the flame is much smaller than the absorption, which is verified based on the calculation of Mie theory.[33] The axisymmetric flame T_1 is divided into 100 ($10\times10\times1$) voxels in the axial, radial, and circumferential directions. Moreover, the non-symmetric flame T_2 is divided into 128 ($4\times4\times8$) voxels. Figure 17 shows the temperature distribution of the axisymmetric (T_1) and the non-symmetric (T_2) flames.

The position and direction of each ray are traced based on the method described in Subsection 2.2. The flame radiative intensity of the ray is calculated by a radiative transfer equation and expressed as[13]

$$I = I_{\mathrm{b},n}[1-\exp(1-\tau_n)] + \sum_{i=1}^{n-1}\left\{I_{\mathrm{b},i}\left[\exp\left(-\sum_{j=i+1}^{n}\tau_j\right)-\exp\left(-\sum_{j=i}^{n}\tau_j\right)\right]\right\}, \tag{15}$$

where I is the radiative intensity, τ is the optical thickness of a flame voxel, and I_{b} is the blackbody radiation intensity under a single spectral condition (with $\lambda = 610$ nm), which is determined according to Planck's law. The noises occurred in the CCD sensor during the flame radiation sampling is also considered. So the Gaussian noise with a signal-to-noise ratio (SNR) of 20 dB is used as measurement errors. The SNR is defined by

$$\mathrm{SNR} = 10\log_{10}\left(\frac{\sqrt{\sum(I_{\mathrm{ccd}})^2}}{\sqrt{\sum(N_{\mathrm{ccd}})^2}}\right), \tag{16}$$

where I_{ccd} is the matrix of the signal value of each pixel on the CCD sensor, and N_{ccd} is the matrix of the noise value added to each pixel.

Figure 18 shows the simulated images of the axisymmetric (T_1) and the non-symmetric (T_2) flames obtained by the commercial and optimized LFCs. In the figure, each pixel of the light field image represents an individual LF sampling.

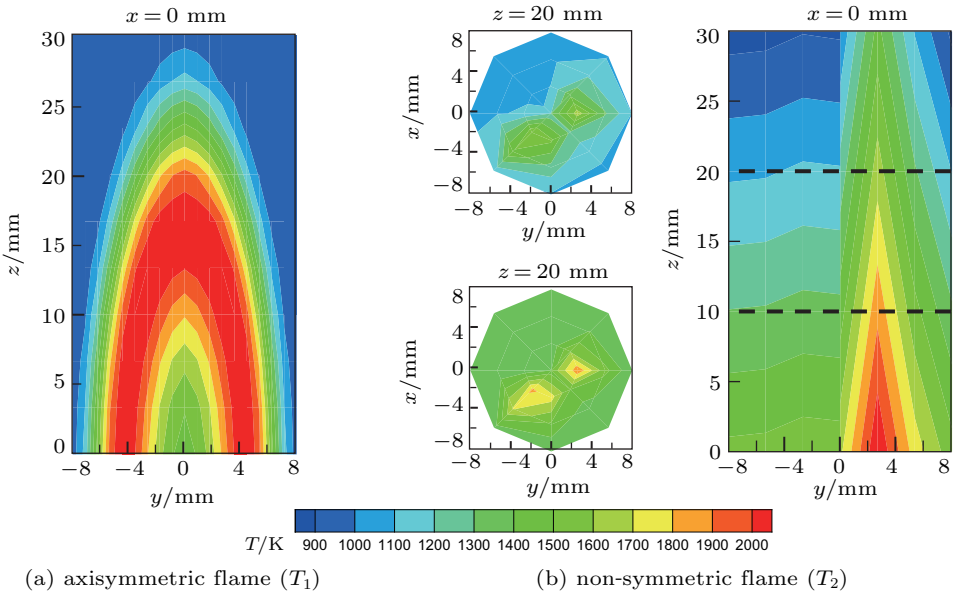


Fig. 17. True temperature distributions of the simulated flames ((a) T_1 and (b) T_2).

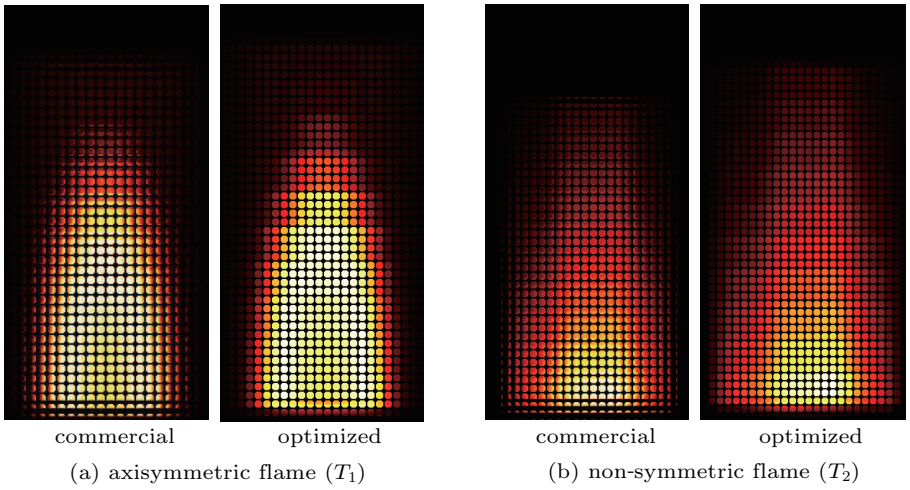


Fig. 18. Simulated flame images obtained by the commercial and the optimized light field cameras. (a) Axisymmetric flame (T_1), (b) non-symmetric flame (T_2).

These LF samplings can be used to obtain the flame radiation intensity of each voxel by the radiation transfer equation

$$I_{\mathrm{ccd}} = A \cdot I_{\mathrm{b}}, \tag{17}$$

where I_{b} is the matrix of the flame radiation intensity of each voxel, and A is the coefficient matrix. An inverse non-negative least square (NNLS) algorithm is applied to solve the I_{b}. The detailed procedures and experimental verification of the NNLS algorithm can be found elsewhere.[20] According to the Planck's law, the temperature (T) of each voxel of the flame can be obtained by

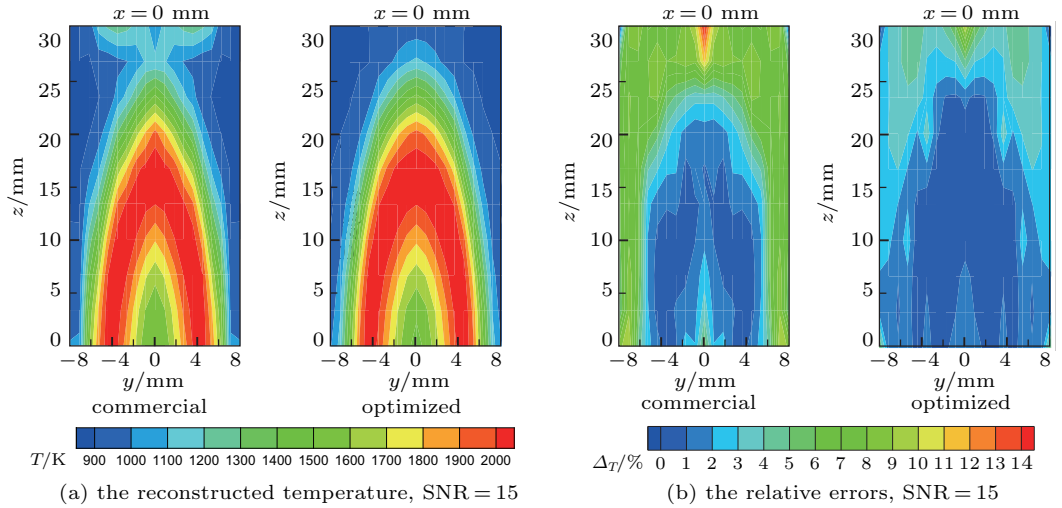
$$T = \frac{hc}{k\lambda} \cdot \frac{1}{\ln\left(\dfrac{2\pi hc^2}{I_{\mathrm{b}}\lambda^5} + 1\right)}, \tag{18}$$

where k is the Boltzmann constant, h is the Planck constant, and c is the speed of light. It is worth noting that the single wavelength condition used here can be achieved by a narrow bandpass filter in the experiments. To evaluate the reconstruction accuracy, the relative error Δ_T is defined by

$$\Delta_T = \frac{T - T_{\mathrm{true}}}{T_{\mathrm{true}}} \times 100\%, \tag{19}$$

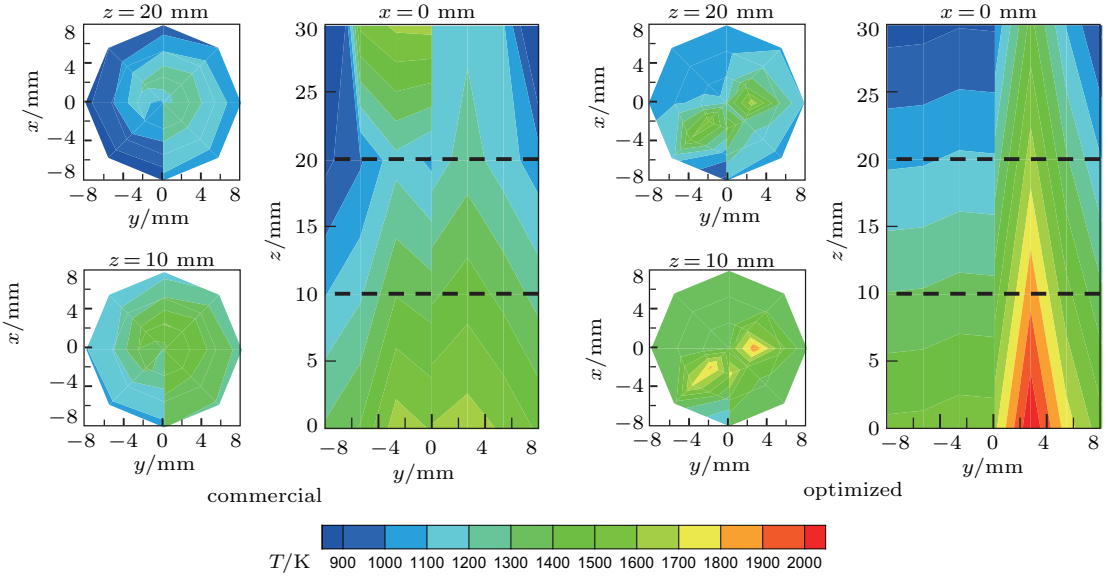
where T is the reconstructed temperature and T_{true} is the true temperature of the corresponding voxel, which is determined by Eqs. (13) and (14).

Figure 19 shows the cross-sections of the reconstructed temperature distribution and the distribution of the relative error of the axisymmetric flame (T_1) for the commercial and proposed parameters of LFCs. The maximum relative error of 14% is found in the tip part of the flame for the commercial LFC while the maximum relative error of 9% is observed for the optimized LFC at the same location.

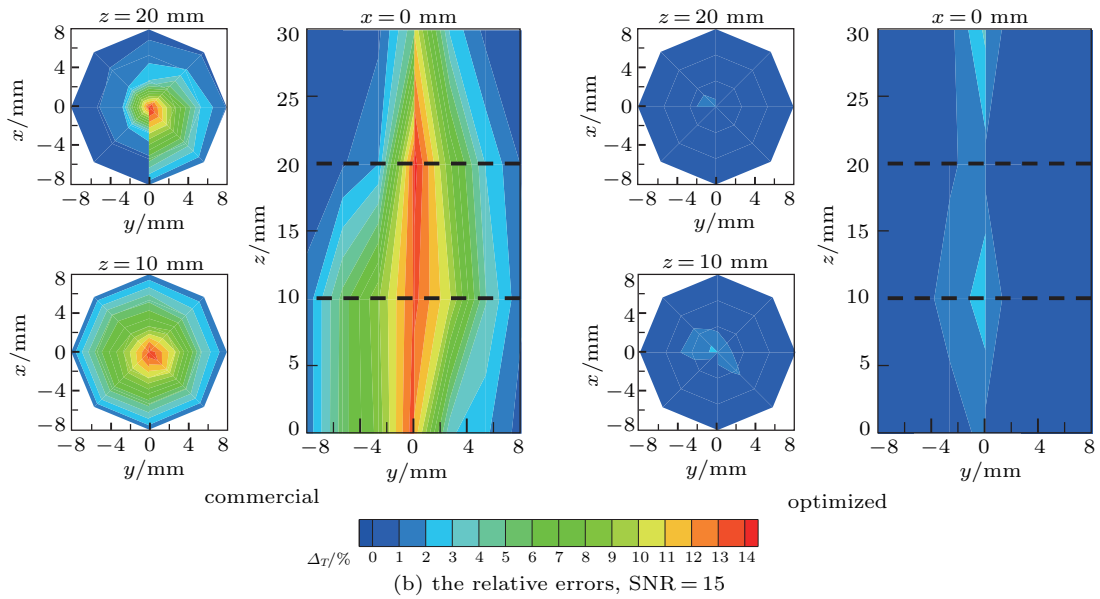


(a) the reconstructed temperature, SNR = 15 (b) the relative errors, SNR = 15

Fig. 19. (a) The reconstructed temperature and (b) relative error distributions of the axisymmetric flame (T_1) for the commercial and the optimized light field cameras.



(a) the reconstructed temperature, SNR = 15



(b) the relative errors, SNR = 15

Fig. 20. (a) The reconstructed temperature and (b) relative error distributions of the non-symmetric flame (T_2) for the commercial and the optimized light field cameras.

Figure 20 shows the cross-sections of the reconstructed temperature distribution and the relative error of the non-symmetric flame (T_2) obtained by the commercial and the optimized LFCs. The temperature reconstruction achieved by the commercial LFC involves significant errors in each cross-section. Also, the area of high temperature cannot be seen clearly compared to the true temperature distribution as presented in Fig. 17(b). The maximum relative error is up to 15% at the center of the flame. It can be concluded that the flame radiation sampled by the commercial LFC is not adequate for the accurate temperature reconstruction of the non-symmetric flame. For the optimized LFC, a more accurate result is obtained with the maximum relative error of 3%.

Comparing between the axisymmetric (T_1) and the non-symmetric (T_2) flame temperature reconstructions, the commercial LFC can perform more accurate measurement on the axisymmetric flame (T_1). On the contrary, the optimized LFC can lower the relative error while measuring the non-symmetric (T_2) flame. Therefore, the standard LFC would be better for the non-symmetric flame while the focused LFC for the axisymmetric flame. It can be concluded that the relative error of the optimized LFC is smaller than that of the commercial LFC. For the optimized LFC, the maximum relative error is lower by 5% and 12% for the axisymmetric (T_1) and non-symmetric (T_2) flame conditions, respectively. This is because the sampling angle of the optimized LFC is increased 23 times compared to the commercial LFC as discussed in Subsection 3.6. Hence, the optimized LFC can provide adequate radiative information for the non-symmetric flame reconstruction. This shows the potential of the optimized LFC to reconstruct a turbulent flame, which is normally non-symmetric. Finally, the results obtained from the numerical simulation suggest that the optimized LFC can provide higher accuracy for the flame temperature reconstruction compared to the commercial LFC.

4. Conclusions

In this study, numerical simulations were carried out to investigate the sampling characteristics of the light field cameras for the flame temperature measurement. The directional and spatial sampling indices of the light field, including cone angle of a single pixel and sampling angle of object side, spatial resolution, and angle of view have been defined to evaluate the sampling characteristics. The effects on the sampling characteristics under different parameters were discussed. Optimized parameters of the LFC were proposed for the flame radiation sampling. The sampling characteristics and indices obtained by the optimized parameters were compared with those of the commercial LFC. A non-negative least square algorithm was used to reconstruct the simulated flame temperature distribution. The concluding remarks obtained from this study are summarized as follows.

(I) The directional sampling accuracy can be varied with the position of the pixel on the CCD sensor. The sampling angle of each pixel also varies with the position of the pixel. The commercial LFC has a uniform sampling characteristic for its all pixels in the field of view. Therefore, the radiation samplings collected by each pixel can be useful for the flame reconstruction.

(II) The better directional sampling accuracy, larger sampling angle, and more directional sampling can be achieved by the standard LFC. In contrast, the better spatial resolution and the larger field of view can be achieved by the focused LFC. Therefore, the standard LFC can be suitable for non-symmetrical flame whereas the focused LFC can be used for the large-scale rotationally symmetrical flame.

(III) It is observed that the longer focal length of the microlens improves the directional sampling accuracy but decreases the sampling angle. Also, the larger magnification of the main lens decreases the directional sampling accuracy and the angle of view but improves the sampling angle and spatial resolution. The increase of the focal length of the main lens decreases the field of view, which has lower impacts on the sampling characteristics. Therefore, the above observations provides the basis to optimize the LFC parameters for the flame radiation sampling.

(IV) It is evident that the larger sampling angle, the wider angle of view, the better directional sampling accuracy, and the higher spatial resolution are needed for the accurate flame radiation sampling. The optimized LFC parameters described in this study are able to improve the light field sampling of the flame radiation. It has been observed that the sampling angle can be increased by 23 times by the optimized LFC in comparison to the commercial LFC.

(V) The results obtained in this study indicate that the optimized LFC can provide better light field sampling for the flame temperature reconstruction, and the higher reconstruction accuracy can be achieved for the symmetrical and non-symmetrical flame conditions.

Further study will focus on the development of the light field imaging system based on the proposed parameters and experimental study.

References

[1] Turns S R 2000 *An introduction to combustion: concepts and applications* (New York: McGraw-Hill)
[2] Ballester J and García-Armingol T 2010 *Prog. Energy Combust. Sci.* **36** 375
[3] Srinivasan K, Sundararajan T, Narayanan S, Jothi T J S and Rohit Sarma C S L V 2013 *Measurement* **46** 315
[4] Dreier T, Chrystie R, Endres T and Schulz C 2016 *Laser-based Combustion Diagnostics* (New York: Wiley)
[5] Xu C L, Zhao W C, Hu J H, Zhang B and Wang S M 2017 *Fuel* **196** 550
[6] Chen X, Yang L X, Xu N, Xie X, Sia B and Xu R 2014 *Opt. Laser Technol.* **57** 318

[7] Wang J, Song Y, Li Z H, Kempf A and He A A 2015 *Opt. Lett.* **40** 1231

[8] Hossain M M, Lu G, Sun D and Yan Y 2013 *Meas. Sci. Technol.* **24** 074010

[9] Levoy M and Hanrahan P 1996 *Proceedings of the* 23*rd annual conference on Computer graphics and interactive techniques* (ACM) pp. 31–42

[10] Adelson E H and Wang J Y A 1992 *IEEE Trans. Pattern Anal. Mach. Intell.* **14** 99

[11] Ng R, Levoy M, Duval G, Horowitz M and Hanrahan P 2005 *Comput. Sci. Tech. Rep.* **2** 1

[12] Lumsdaine A and Jose S 2009 *IEEE International Conference on Computational Photography* pp. 1–8

[13] Sun J, Xu C L, Zhang B, Hossain M M, Wang S M, Qi H and Tan H P 2016 *Opt. Express* **24** 1118

[14] Sun J, Xu C L, Zhang B, Liu Y D and Wang S M 2017 *J. Eng. Thermophys.* **38** 2164

[15] Sun J, Hossain M M, Xu C L, Zhang B and Wang S M 2017 *Opt. Commun.* **390** 7

[16] Niu C Y, Qi H, Huang X, Ruan L M and Tan H P 2016 *J. Quant. Spectrosc. Radiat. Transf.* **184** 44

[17] Huang X, Qi H, Niu C Y, Ruan L M, Tan H P, Sun J and Xu C L 2017 *Appl. Therm. Eng.* **115** 1337

[18] Bolan J T, Johnson K C and Thurow B S 2014 *Proceedings of* 30*th AIAA Aerodynamic Measurement Technology and Ground Testing Conference* pp. 1–12

[19] Li T J, Li S N, Yuan Y, Wang F Q and Tan H P 2018 *Int. J. Heat Mass Transf.* **119** 303

[20] Sun J, Hossain M M, Xu C L and Zhang B 2018 *Int. J. Heat Mass Transf.* **121** 1281

[21] Niu C Y, Qi H, Huang X, Ruan L M, Wang W and Tan H P 2015 *Chin. Phys. B* **24** 114401

[22] Wetzstein G, Ihrke I, Lanman D and Heidrich W 2011 *Comput. Graph. Forum* Vol. **30** (New York: Blackwell Publishing Ltd) pp. 2397–426

[23] Chai J X, Tong X, Chan S C and Shum H Y 2000 *Proceedings of the* 27*th annual conference on Computer graphics and interactive techniques* (New York: Addison-Wesley Publishing C) p. 307

[24] Lumsdaine A, Georgiev T G and Chunev G 2012 *Proceedings of of SPIE-IS&T Electronic Imaging* Vol. **8299** p. 829909

[25] Iglesias I and Ripoll J 2014 *Opt. Express* **22** 23215

[26] Philipp K, Koukourakis N, Kuschmierz R, Leithold C, Fischer A and Czarske J 2015 *Opt. Lett.* **40** 514

[27] Ndo T A, Horisaki R and Tanida J 2015 *Appl. Opt.* **54** 7316

[28] Hecht E 2001 *Optics* Vol. **1** (New York: Addison Wesley)

[29] Lei Y, Tong Q, Xin Z W, Wei D, Zhang X Y, Liao J, Wang H W and Xie C S 2017 *Rev. Sci. Instrum.* **88** 033111-1

[30] Georgiev T and Lumsdaine A 2009 *Eurographics* pp. 5–8

[31] Liu H W, Zheng S and Zhou H C 2017 *IEEE Trans. Instrum. Meas.* **66** 315

[32] Liu G N and Liu D 2018 *Chin. Phys. B* **27** 054401

[33] Felske J D and Tien C L 1973 *Combust. Sci. Technol.* **7** 25